



# Universiteit Leiden

MASTER OF SCIENCE - Academic Year 2019/ 2020

Astronomy and Data Science

## 1<sup>st</sup> Research Project

### A quest for fossil radio plasma in galaxy clusters

Author:

Margherita Grespan

Student ID:

2233150

Supervisors:

Dr. Reinout van Weeren  
MSc. Gabriella Di Gennaro

---

## Abstract

In this thesis we will carry out a search for old fossil radio plasma from previous episodes of AGN activity in the galaxy cluster MKW8 ( $z = 0.027$ ). Recently, it has been realized that AGN fossil plasma might play an important role in many particle (re-)acceleration processes that take place in galaxy clusters. However, the scenario of galaxy clusters is complex and the diffuse radio sources present have different shapes and proprieties which are difficult to fit into a precise category. To characterize the properties of the diffuse radio emission in MKW8, we analyze 1.5 GHz Very Large Array (VLA) observations. We complement these data with 325 MHz Giant Metrewave Radio Telescope (GMRT) and 150 MHz LOw Frequency ARay (LOFAR) observations. We carry spectral index and polarization studies. The diffuse radio emission shows an ultra-steep spectrum,  $\alpha \sim -2.40 \pm 0.17$ , and we set an upper limit to its degree of polarization,  $p = 0.8\%$ . These results, combined with the small size of the source (about 100 kpc), the location close to the cluster center, and the filamentary structure, made us classify it as a radio phoenix.

# 1 Introduction

## 1.1 Galaxy clusters

Galaxy clusters are the largest gravitationally bound systems in the Universe, with typical masses of about  $10^{15} M_{\odot}$ . They can hold hundreds of galaxies - up to several thousands - in their potential well within a radius of 1–2 Mpc (Markevitch & Vikhlinin, 2007). However, most of the gravitating matter (around 80%) is in the form of dark matter (Blumenthal et al., 1984) whose nature is still not understood.

Clusters form via a hierarchical sequence of major and minor mergers. They grow through the accumulation of small groups of galaxies or merging with other clusters (Springel et al. (2006), Press & Schechter (1974)). Those kinds of merger events are very energetic, a huge amount of gravitational energy  $\sim 10^{64} \text{ ergs}$  is released on a Gyr timescale (Kravtsov & Borgani, 2012). Part of this energy is consumed in form of gas<sup>1</sup> heating, shocks and turbulence (shocks: Miniati et al. (2000)). The dissipation of a huge amount of kinetic energy is also likely to accelerate particle populations up to relativistic energies<sup>2</sup> on the cluster scales (Brunetti & Jones, 2014), generate density and temperature jumps (Markevitch & Vikhlinin, 2007) and amplify the magnetic field.

Consequently, in literature, clusters are divided in *relaxed*, i.e. dynamically undisturbed systems, and *merging*, i.e. systems that show signs of dynamical activity.

## 1.2 Multiwavelength cluster emission

Multiwavelength studies are needed to understand the structure of a cluster. The combined information from optical, radio and X-ray observations are necessary to have an overall picture of cluster components.

Electromagnetic radiation is emitted by accelerated charged particles. Thus, two kind of processes are possible: *thermal* emission which only depends on the temperature of the emitting object and *non-thermal* emission which is not related to the temperature of the object. Thermal emission is due to particle motion. Every object above 0 K has some internal motion and therefore emits thermal radiation. Non-thermal emission, instead, is due to the interaction of ultra-relativistic particles and magnetic field, i.e. *synchrotron radiation* which emits in the radio frequencies.

In galaxy clusters, the main processes which occur are thermal bremsstrahlung and synchrotron radiation.

**Thermal Bremsstrahlung** In general, bremsstrahlung radiation is the radiation emitted by a charged particles when accelerated - deflected - by an electric field. When deflected, a moving particle loses velocity, hence kinetic energy and, to satisfy the law of conservation of energy, a photon is emitted. During this kind of interaction, the acceleration is not constant therefore the photons are emitted with a range of wavelengths, i.e. a continuum spectrum. When considering a population of electron with a certain temperature, i.e. internal motion, the total emission by all particles of a population is called thermal bremsstrahlung.

---

<sup>1</sup>The ICM, see sec. 1.3.1

<sup>2</sup> particles with a Lorentz factor  $\gamma > 1000$

**Synchrotron Radiation** When an ultra relativistic charged particle travels through the magnetic field it spirals along the field lines in helical paths. This change in direction cause an acceleration and therefore electromagnetic emission. This process, named Synchrotron Radiation, is very common in radio astronomy - [De Young \(1984\)](#) for a complete review on the physics of extra-galactic radio sources. Moreover, usually, *incoherent synchrotron radiation* comes from an ensemble of ultra-relativistic electrons<sup>3</sup> (plasma) accelerated by a magnetic field.

The observed spectrum of Synchrotron emission is the sum of the emission spectra from the individual electrons, and is described by a power law spectrum:

$$S_\nu \propto \nu^\alpha \quad (1)$$

with  $S$  flux,  $\nu$  frequency and  $\alpha$  spectral index. This relation becomes linear in a logarithmic space,

$$\log S_\nu = \alpha \log \nu + C \quad (2)$$

Depending on the value of the spectral index  $\alpha$  the sources are distinckted.

When a source has  $\alpha \sim 0$  it is called flat spectral index, with  $\alpha < 0$  negative and  $\alpha \ll -1$  steep. The spectral index of a source is not constant. In fact, with time, the accelerated electrons lose energy under radiative losses which lead to a steepening of the spectrum ([Rybicki & Lightman \(1979\)](#) for a complete review).

In literature, *spectral index maps*, i.e. how  $\alpha$  varies in the image, are widely used to analyze the proprieties of the celestial sources and their emission process. Also, the synchrotron emission is usually highly polarized, whose degree and orientation give information about the magnetic fields of the source.

### 1.2.1 Optical wavelengths

**1.2.1.1 Galaxies** The first cluster detection have been done in the optical wavelengths. Optical cluster surveys have been created observing galaxy population overdensities to define the individual clusters. However, optical observations are vulnerable to projection effects.

In a cluster, only around 3-5% of the gravitating matter is constituted by galaxies, which is also the luminous part. More precisely, galaxies are formed by stars whose emit Black body (BB) radiation and the combination of those signals creates a BB continuum signal spanning a range in temperatures, observable in optical wavelenght.

Clusters contain a majority of Elliptical (E) and Lenticular (S0) galaxies. Nonetheless, there is one type of galaxies which is more interesting than the others. Most of the clusters host a massive *brightest cluster galaxy*, or *BCG*, at their core. BCGs have typical luminosities 10 times higher than those of 'normal' galaxies in the cluster, furthermore, their masses are about  $10^{13} M_\odot$  which is comparable to the mass of a galaxy group ([Katayama et al., 2003](#)). Among all cluster galaxies, the BCG is most likely the most massive one and has the biggest impact on the ICM (see Intra-Cluster Medium in sec. [1.3.1](#)) properties ([Sun, 2009](#)). Furthermore, they are believed to play an important role in regulating the rate at which gas cools at the core of the clusters ([Von Der Linden et al., 2007](#)). More precisely, BCG often hold active galactic nuclei (e.g. [Burns \(1990\)](#)), which may provide the necessary heating to counteract radiative cooling. However, the nature and the classification of those galaxies is still debated.

---

<sup>3</sup>electrons with a Lorentz factors of  $\sim 10^4$

## 1.3 X-ray wavelengths

### 1.3.1 Intra-Cluster Medium

The intracluster medium (ICM) is diffuse matter that pervades the space between the galaxies over the cluster volume. This diffuse ( $10^3$  particles  $\text{cm}^{-3}$ ) hot gas ( $10^7\text{-}10^8$  K) represent the  $\sim 15\text{-}17\%$  of the total cluster mass (Mitchell et al. (1976), Forman & Jones (1982)) and constitute most of the cluster baryonic<sup>4</sup> content ( $\sim 75\%$ ). Given the high temperature, the ICM is fully ionized and electrons and ions interact through their electric fields. These interactions decelerate the electrons with a subsequent emission of high-energy radiation (thermal Bremsstrahlung) which is detectable in the X-ray energy band.

### 1.3.2 Radio wavelengths

**1.3.2.1 Radio Galaxies** Radio galaxies have sizes in a range from few pc to Mpc. Their optical counterpart is usually an elliptical galaxy with a supermassive black hole (BH) ( $M_{BH} \sim 10^7 - 10^9 M_\odot$ ) in their core. Single galaxies in clusters are radio emitters as the ones found outside the cluster gravitational well. However, galaxies in cluster show peculiar non symmetrical-shapes. This is probably due to the interaction with the ICM and the cluster potential well.

In general, galaxies diffuse radio emission comes from synchrotron emission due to cosmic ray electrons spread over the galactic disk and halo. Moreover, synchrotron emission it is usually produced in black holes magnetic fields (AGNs). Radio maps show the main features of galaxies morphology. In detail, we find *jets* coming from either side of a compact nucleus, which then develop towards extended components known as *lobes* or *tails* and *hotspots* which are placed at the end of the jets. Jets, more precisely, trace the path of the material ejected from active galactic nucleus - accreted matter in the black hole disk.

Using spectral index maps it is possible to analyze the history of a galaxy. Those maps usually show a flat  $\alpha$  in the center - radio core - where the particles have just been accelerated and, for this reason, defined as young. Moving out to the radio tails,  $\alpha$  becomes steep since old plasma is present. On the other side, on the hotspots the particles show a spectral index of a young population. This is due to the re-acceleration after an interaction - shock - with the ICM. We see that each component has a different spectral index depending on the processes shaping the diffuse synchrotron emission. For example, the just mentioned steepening of the spectrum away from the disk is an indication of loss processes during the propagation of cosmic ray electrons in the halo.

### 1.3.3 Diffuse radio sources

In addition to discrete radio emission from galaxies, we also detect diffuse radio emission. This is principally due to two main factors. The magnetization of the ICM (detected through the *halos*) and the presence of accelerated particles - everywhere - over the cluster scale. In *disturbed* cluster we can find cluster-scale synchrotron emission, these kind of emitting sources are indeed named *diffuse radio sources*.

In radio astronomy diffuse radio sources are sources which are not clearly associated with a particular

---

<sup>4</sup>protons, neutrons and all the objects composed of them (i.e. atomic nuclei)

optical host. Diffuse *cluster* radio sources have been divided into three main classes - *halos*, *minihalos* and *relics* - based on their location in the cluster, the type of cluster, and their size (Feretti & Giovannini, 1996).

**Halos** Cluster radio halos are centrally located diffuse extended ( $\gtrsim 1$  Mpc) radio sources of low surface brightness in merging cluster. They arise in turbulent gas area where electrons are continuously accelerated (Brunetti & Jones, 2014). Halos do not have a strict connection to other sources, *i.e.* they do not have an optical counterpart - (Cassano et al. (2010), Cuciti et al. (2015), Kale, R. et al. (2015)) but their brightness generally follows the distribution of the thermal emitting (X-ray) ICM. The total radio spectra of halos are steep ( $\alpha \approx -1, -1.5$ ) with a steepening at higher frequencies, as frequently found in aged radio sources (see Feretti (2005), Feretti et al. (2012) for a complete description of non-thermal diffuse emission).

**Minihalos** Minihalos are small sizes (few hundred kpc) roundish diffuse radio sources and are present in relaxed cool core clusters which also host a powerful radio galaxy associated with the BCG (see Gitti (2015) for an overview on mini-halos). Since Minihalos are found in cooling cores of relaxed clusters are the only diffuse sources not correlated to a merger event.

**Relics** Other similar extended ( $\sim 1$  Mpc) sources, found at the cluster periphery, but with elongated morphology and strong radio polarization are the *radio relics* (Govoni et al., 2001). Radio relics are typically found to trace re-accelerated particles by shock-waves. Furthermore, relics give an indication of the magnetic field and relativistic particles in the cluster outskirts.

Relics can be distinguished in two categories, as suggested by Kempner et al. (2004): *Radio phoenix* if associated with an AGN activity (sources that trace AGN radio plasma) or *Radio Ghosts* if related to the ICM. In order to follow this classification the origin of the source has to be known, but obviously, this is not always possible so relics can also be distinguished by their morphology, *i.e.* *elongated* and *roundish*.

**Phoenices** Phoenices are object of interest in now-a-days astronomy, e.g. Slee et al. (2001), van Weeren, R. J. et al. (2011), Kempner et al. (2004), de Gasperin et al. (2015), Mandal et al. (2019), Mandal et al. (2019), and with this work we try to get a further insight of this not well understood type of extended sources.

Radio phoenices are a not-well known kind of extended sources in galaxy clusters. In this discussion we will adopt the Kempner et al. (2004) classification in which phoenices are thought to be AGN fossil plasma compressed and revived by merger shocks waves which boost the radio emission (van Weeren et al., 2019). Enßlin, T. A. & Gopal-Krishna (2001) simulated that plasma which remains intact after the release, *i.e.* not older than 2 Gyr, can be revived. The result is a source characterized by a steep radio spectra with complex morphologies (Enßlin & Brüggen, 2002).

The candidates for the fossil electrons are the lobes and tails of radio galaxies, which have an ultra steep spectra, as we expect, due to aging. Aging is due to synchrotron losses of energy of relativistic electrons after the cessation of the injection of fresh particles into the radio lobes (Komissarov & Gubanov, 1994). An adiabatic compression seems the most likely process to re accelerate fossil particles (Enßlin & Brüggen (2002), Enßlin & Brüggen (2001)). Not a lot of phoenices have been observed at

low-frequency observations of cluster (e.g. [Slee et al. \(2001\)](#), [Kempner et al. \(2004\)](#), [de Gasperin et al. \(2015\)](#), [Mandal et al. \(2019\)](#)). Nonetheless, radio phoenixes are found at small cluster centric distances ([Feretti et al., 2012](#)), and have a spectral index steeper than -1.5, i.e.  $\alpha < -1.5$ . However a direct observational evidence for a connection between fossil plasma, adiabatic compression and phoenix creation is still missing.

## 1.4 MKW 8

In this work we study the properties of the diffuse radio emission present in the galaxy cluster MKW8. For this study we used observation of the galaxy cluster MKW8 obtained with LOFAR at 150 MHz, GMRT at 325 MHz and VLA at 1.5 GHz. Telescopes characteristics are described respectively in sec. [2.2](#), [3.2.1](#), [3.2.2](#).

MKW8 is a poor galaxy cluster part of the HIFLUGCS (HIghest X-ray FLUx Galaxy Cluster Sample, ([Reiprich & Bohringer, 2002](#))) at redshift  $z = 0.0270$  ([Lin & Mohr, 2004](#)) which gives a scale of 0.543 kpc/'' assuming the  $\Lambda$ CDM Cosmology. Where throughout this work, we assume  $H_0 = 70 \text{ km s}^{-1} \text{Mpc}^{-1}$ ,  $\Omega_m = 0.3$ , and  $\Omega_\Lambda = 0.7$ . All sky coordinates are epoch J2000 coordinates.

MKW8 is classified as a non-cooling cluster (NCC) with a central cooling time of MKW8  $t_{cool} = 10.87 \text{ Gyr}$  ([Hudson et al., 2010](#)) at  $r = 0.4\%R_{500}$ <sup>5</sup>, and it also presents a central radio source ([Bharadwaj et al., 2014](#)). Non-cooling clusters are characterized by an X-ray temperature profile that does not fall towards the center. This probably happens because those type of clusters are still dynamically active, implying a centrally cooling time exceeding the Hubble time.

Given a  $M_{500}=0.735\times10^{14} \text{ M}_\odot$ <sup>6</sup>, ([Piffaretti et al., 2011](#)) obtained  $R_{500}=0.631 \text{ Mpc}$ . In its potential well with MKW8 contains 183 galaxies ([Zhang et al., 2011](#))<sup>7</sup>. The core<sup>8</sup> metallicity weighted average over a shell  $r < 0.15 R_{500}$  is  $Z \sim 0.5 Z_\odot$  with an X-ray temperature  $kT \sim 2.5 \text{ keV}$  ([Elkholy et al., 2015](#)). The BCG of the cluster is NCG 5718 ([Lin & Mohr, 2004](#)) with coordinates RA=14:40:42.81 DEC=+03:27:55.3 (J2000) ([Zhang et al., 2011](#)).

The cluster is gravitationally bound to MKW7 and [Beers et al. \(1995\)](#) showed how likely is a merge in the next several Gyrs. Recently, [Tümer et al. \(2019\)](#) explored the X-ray properties of the intracluster medium of MKW8 and BCG corona in order to understand the role of the BCG in the cluster evolution. In this work we are interested to the mechanism that created the diffuse radio emission present in the cluster which seem positioned close to the BCG.

## 2 Introduction to Radio Astronomy

Radio astronomy is the study of the radio emission from celestial bodies. Almost every object emits radio waves of some length. Radio waves are detected using antennas and in particular with aperture-

---

<sup>5</sup> $R_{500}$  is the radius within which the mass density is 500 times the critical density of the Universe ( $\rho_c$ ), at the cluster redshift, which represents the average density of matter required for the Universe to be in balance - halt its expansion, i.e.  $\rho_c(z) = \frac{3H^2(z)}{8\pi G}$ .  $R_{500}$  is computed spherical symmetry, i.e.  $M_{500} = \frac{4}{3}\pi R_{500}^3 \rho_{c,500}$ , with  $\rho_{c,500} = 500\rho_c$ .

<sup>6</sup>MCXC catalogue: <http://cds.u-strasbg.fr>

<sup>7</sup>The authors selected galaxies with redshifts within an aperture of at least 1.2 Abell radius, i.e., 2.57 Mpc, centered on the BCG. Then based on the line-of-sight velocity of the galaxy as a function of its projected distance from the BCG they decided the cluster members. Additional information in [Diaferio \(1999\)](#) and [Zhang et al. \(2011\)](#)

<sup>8</sup>Inner part of the cluster

synthesis interferometers constructed using coherent amplifiers. The radio band is very broad, it spans from 10 MHz (30 m) to 1 THz (0.3 mm). The range limit is due to the absorption of the free electrons in the ionosphere (at low frequencies) and to the absorption of the water vapour (at high frequencies). In this work we used L-band (1–2 GHz, see Tab. 2, for more info about this frequency range in the radio spectrum) observations of the MKW8 cluster using the Very Large Array telescope (see Sec. 2.2).

## 2.1 Radio telescopes

The radio band is very wide and the sensibility of a telescope depends on the area and efficiency of the antenna. In general, in order to retrieve signal from the weakest sources large antennas are needed. Throughout this section we will explain how a radio telescope works and why interferometry is needed in astronomy.

### 2.1.1 Single dish antenna

The purpose of an antenna is to capture radiation from an object and couple it to a receiver for detection, digitization, and analysis.

An isotropic radio antenna is described by its *collecting area*, namely the power received per unit solid angle in direction  $(\theta, \phi)$ , which has the same gain<sup>9</sup> in all directions. The larger the antenna's dish, i.e. the larger its collecting area, the fainter the sources that can be detected. The effective collecting area  $A_e(\theta, \phi)$  of any antenna averaged over all directions  $(\theta, \phi)$  is

$$\overline{A_e} = \frac{\lambda^2}{4\pi}, \quad (3)$$

where  $\lambda$  is the wavelength in which we are observing.

The shape of the antenna's signal is characterized by a *primary beam* (PB), i.e where radiation is mainly sensitive to, and it is defined as the region containing the principal response out to the first zero. Outside of this region there are the *side lobes* which can be interpreted as the diffraction pattern of the antenna. The purpose of data deconvolution is to minimize side lobes and maximize the signal contained in the main beam.

The resolution of a single dish telescope, i.e. the minimum angular distance between two distinguishable objects in an image is:

$$\theta_{rad} \approx \frac{\lambda}{D} \quad (4)$$

where  $D$  is the diameter of the dish.

In order to achieve sub-arcsecond resolution in the radio band the diameter of the dish would be impossibly large. For example, in order to have 1 " resolution at 1.5 GHz we would need a 41.2 km dish. In order to overcome this limitation, astronomers use the *aperture synthesis*, i.e. the technique of synthesizing a larger aperture through combinations of separated pairs of antenna. This technique is used in interferometers.

---

<sup>9</sup>The *gain* of a receiving antenna is its efficiency to transform radio waves (the signal) into electrical power.

### 2.1.2 Interferometers

An interferometers is defined as a collection of single antenna. With the coherent interferometry, the spatially separated signal can be correlated. In this way two antennas simulate a single dish with a diameter equal to their distance. In particular, Eq. 4 then becomes:

$$\theta_{rad} \approx \frac{\lambda}{b} \quad (5)$$

with  $\lambda$  the observed wavelength and  $b$  the distance between the antennas, called *baseline*. The signal from the observed source arrives at each antenna at different time. This is due to the different travel lengths which depends on the position of the antenna in the array. This phase delay is expressed as:

$$\phi = \frac{2\pi}{\lambda} \cdot B\vec{s} \quad (6)$$

where  $B$  is the baseline vector between each pair of antenna,  $\vec{s}$  is the unit vector in direction of the source. As said above, the signals arrive at different time at each antenna and this provides positional information about the emitting object. This happens in the correlator, where the time delay is measured and compensated for in the software. Basically, the interferometer measures the interference pattern produced by multiple apertures - collected signals from every antenna.

The output signal from the interferometer is the so-called *visibility function*  $V(u, v)$  (in function of the baseline coordinates  $u$  and  $v$ ):

$$V(u, v) = \int \int I(l, m) e^{-i2\pi(ul+vm)} dl dm, \quad (7)$$

where  $I(l, m)$  is the *sky brightness (intensity) distribution* in function of the sky coordinates  $(l, m)$ . The image of the sky can therefore be obtained by inversion of the Fourier Transformation of Eq. 7:

$$I(l, m) = \int \int V(u, v) e^{i2\pi(ul+vm)} du dv \quad (8)$$

In a real case, the sky image, *i.e.* Eq. 8, is impossible to retrieve without missing information. This is due to the limited number of antennas, and consequently the limited number of baselines<sup>10</sup>, which do not fully cover the full  $u-v$  plane. To overcome information leaking, a *sampling function*,  $S(u, v)$ , is used. This function is equal to 1 in the  $u-v$  plane<sup>11</sup>, and it is 0 elsewhere. Equation 7 is true only in the case where all the possible values of  $u$  and  $v$  are sampled. The measured visibility can be expressed as:

$$V_M(u, v) = S(u, v)V(u, v). \quad (9)$$

The dirty image is defined as the convolution of sky with “dirty beam”  $B$ :

$$B(l, m) = \int \int S(u, v) e^{2\pi i(ul+vm)} du dv \quad (10)$$

$$I_D(l, m) = B(l, m) * I(l, m) \quad (11)$$

To recover  $I(x, y)$ , we must deconvolve  $B(x, y)$  from  $I_D(x, y)$ . In order to do that we will use the CASA software (Sec. 3.3.3).

---

<sup>10</sup>the number of baselines is given by  $N_b = \frac{(N^2 - N)}{2}$ , with  $N$  the number of antennas.

<sup>11</sup>Visibilities are observed only at discrete locations.

## 2.2 The VLA

The *Very Large Array* (VLA<sup>12</sup>) is an imaging radio interferometer located in central New Mexico, operated by the *National Radio Astronomy Observatory* (NRAO<sup>13</sup>). The telescope is composed of 27 antennas of 25 meter diameter positioned along three Y shaped arms of 21 km length (see Fig. 1; more details about how the VLA works can be found in Perley et al. (2011)). Each antenna lays on a double railroad tracks, which allows to change the antennas’ position, *i.e.* the baseline’s length. The VLA has four basic antennas arrangements, A through D, characterized by different baselines lengths (see Table 1). The shift of the baseline affects the observations resolution: the *maximum* baseline length ( $B_{max}$ ) determines the resolution ( $\theta = \lambda/B_{max}$ ), while the *minimum* baseline length determines the sensitivity to large scale features (a source is resolved if the angular size is  $> \lambda/B_{min}$ ). This means that an interferometer is sensitive to a range of angular sizes:

$$\frac{\lambda}{B_{max}} < \theta < \frac{\lambda}{B_{min}}. \quad (12)$$

The A-array configuration has the longest baselines, hence it provides the highest angular resolution. However, its sensibility to surface brightness is not high. On the other side, the D-array configuration has the shortest baseline, so it is sensible to a high surface brightness lacking on angular resolution.

**Table 1:** Maximum and minimum antenna separations for each configuration of the VLA.

Configuration	$B_{max}$ (km)	$B_{min}$ (km)
A	36.4	0.68
B	11.1	0.21
C	3.4	0.035
D	1.03	0.035

The VLA antennas are equipped with 8 receivers, permitting a 1–50 GHz frequency coverage. In Table 2 the characteristics of the 1–2 GHz (L-band), *i.e.* the observing band of the dataset used in this work, are reported. The L-band is divided in 16 subbands to cover the entire frequency range. The 16 subbands are also named spectral windows (*spw*), and are enumerated (from 0 to 15) in increasing frequency order. Each spectral windows is further divided into channels.

---

<sup>12</sup><http://www.vla.nrao.edu/>

<sup>13</sup><https://public.nrao.edu/>

**Table 2:** Basic information about the VLA L-band observations.

L band	
Frequency (GHz)	1.0-2
Wavelenght (cm)	20
Primary beam (arcmin)	30
Highest resolution (arcsec)	1.4
System Temperature (K)	37-75



**Figure 1:** A photograph of the VLA in his most compact configuration (*D*-array), which has 1 km as maximum baseline. It is possible to spot the rail lines used to move the antennas.

### 3 Observations and data reduction

The data reduction has been made with the use of the Common Astronomy Software Applications - CASA<sup>14</sup> (McMullin et al., 2007) software version 5.6.0-6.0.

#### 3.1 The dataset

The cluster has been observed with three different VLA configurations, i.e. B, C and D, in a period from June to May 2017. The three VLA configurations are described in Tab. 1 and the observation dates and observing time (on-source) are included in Tab. 4.

#### 3.2 Additional datasets

In our study of MKW8 complementary datasets have been used in order to produce a spectral index image (Sec. 4.2.1). We will not discuss in detail the structure of the additional telescopes since for this study we used only the final (i.e. calibrated) images.

---

<sup>14</sup><https://casa.nrao.edu/>

**Table 3:** Observation date for each configuration and the relative on-source time. The on-source time is the amount of time the target has been observed.

Configuration	Observation date	On-source time
B	June 25, 2017	2 h
C	February 23, 2017	5 h
D	May 26, 2017	2 h

**Table 4:** Information on the observation taken with the VLA. Column: (1) source name; (2) VLA configuration; (3), (4) source coordinates; (5) optical classification of the source; (6) source redshift.

Source	Array	RA (J2000)	DEC (J2000)	Optical ID	Redshift $z$
MKW8 <sup>1</sup>	B,C,D	14 h 40 m 38 s	+3° 8' 35"	cluster	0.027
J0713+4349 <sup>2</sup>	B,C	7 h 13 m 38. s	+43° 49' 17"	galaxy	0.518
J1445+0958 <sup>3</sup>	B,C,D	14 h 45 m 16 s	+9° 58' 36 "	quasar	3.535
J1331+3030=3C286 <sup>4</sup>	B,C,D	13 h 31 m 8 s	+30° 30' 33"	quasar	0.846
J0542+4951=3C147 <sup>2</sup>	C	5 h 42 m 36 s	+49° 51' 7 "	quasar	0.545

<sup>1</sup> target

<sup>2</sup> amplitude, bandpass, phase, polarization calibrator

<sup>3</sup> amplitude and phase calibrator

<sup>4</sup> bandpass, flux, phase, polarization angle calibrator.

### 3.2.1 GMRT

The Giant Metrewave Radio Telescope (GMRT) is one of the largest and most sensitive low-frequency radio telescopes in the world (Gupta et al., 2017). The array configuration is composed of 30 antennas, each of 45 m diameter, and a longest baseline of 25 km. The array operates at six frequencies, centered at 50, 153, 233, 325, 610 and 1420 MHz.

In this study we will use a 325 MHz observation (Project Code: 17\_073, PI: A. Edge) of the MKW8 cluster.

### 3.2.2 LOFAR

The Low Frequency Array (LOFAR, van Haarlem, M. P. et al. (2013)) is the largest radio telescope operating at the lowest frequencies observable from the ground, *i.e.* is constructed for astronomical observations below 250 MHz.

The telescope is composed by two types of antenna, The Low Band Antenna (LBA) which operates between 10 and 90 MHz and the High Band Antenna (HBA) between 110 and 250 MHz. In this work we will use an observation (Project Code LC11\_015; PI: S. Mandal) in the HBA frequency range, with central frequency at 150 MHz.

Differently to the VLA, LOFAR has omni-directional dipoles as elements of the phased array at individual stations. Furthermore, the signal from the separate antennas is digitized and sent to central

digital processor, which combines them emulating an interferometer.

### 3.3 Calibration

The first step in the data analysis is the data calibration. Every signal is noisy for instrumental and environmental effects. This is because the visibility is corrupted by diverse factors, namely Radio Frequency Interference (RFI), Antenna/Receiver/Correlator failures, bad weather and shadowing. The calibration is the effort to measure and remove the time-dependent and frequency-dependent atmospheric and instrumental variations. The data calibration is applied separately to each configuration, i.e. the B-, C- and D-array.

#### 3.3.1 External calibration

We start with the external, or *a-priori*, calibration. This calibration makes use of known sources, called calibrators, in order to correct the data. The calibrators used in this observation are reported in Table 4.

The first steps of data calibration consists on removing the ranges affected by shadowing or Gibbs phenomenon<sup>15</sup> - radio inference - and estimating the gain of the target source with the calibrators (see Tab 4).

**3.3.1.1 Calibrators** Calibrators are bright and isolated sources whose position and intensity are known ([Ollier, 2018](#)). They are usually point sources, this permits to easily predict their visibilities since amplitude can be approximate constant and phase  $\sim 0$ ).

Several kinds of calibrators, with different purposes, exist and they are:

**Primary - Amplitude - calibrators** Visibility amplitude calibrators are needed to solve the irregularities in the signal due to non-identical electronics of the antenna. The primary calibrator is a bright source with known flux-density, spectral bandpass and polarization fraction. With this source is possible to scale relative amplitudes to absolute value. In our observation the source 3C286 is the amplitude calibrator, see Table 4. This source is the last one to be observed in the overall observing schedule.

**Secondary - Phase - calibrators** The phase calibrators are used to solve the signal variations due to ionosphere or troposphere effects, respectively, at low ( $< 10$  MHz) and high ( $> 1$  GHz) frequencies ([Olmi, 2002](#)). An ideal secondary calibrator is a strong, compact and close to the target source.

The calibrator is observed periodically during the observing schedule permitting an estimate of local conditions. The calibrator fluctuations are related - and then corrected - to the target source whose proprieties are unknown. Calibrators are also used for other purposes. Some of them are assumed to be unpolarized and used to determine the polarization terms. Sometimes primary calibrators can also

---

<sup>15</sup>The *Gibbs phenomenon* describes the creation of an artifact when a function with a jump discontinuity is estimated with the use of a Fourier series. In an image, the Fourier transformation of sharp edges results in many high spatial frequencies.

be used to calculate the spectral bandpass<sup>16</sup> and the channels polarization angles dependence. The Bandpass calibrator fixes instrumental effects and variations *vs* frequency.

### 3.3.2 External calibration in CASA

External calibration starts with the removal of the ringing (Gibbs phenomenon) across the frequency channels of the observation. More precisely, to handle a source affected by interference, we use the task `hanningsmooth` in CASA which smooths the sources edges in order to reduce the typical ringing. The Gibbs phenomenon is not the only type of Radio Frequency Interference: data can be corrupted also by transmitters noise, lightning, solar activities and internal (circuit) noise.

Secondly, we face another issue without the use of the calibrators. Depending on the configuration or the elevation of the observed source, some antenna are blocked (shadowed) by other antennas in the array during the observation time. Knowing this, it is possible to "hide" the data for certain antenna in a precise range of time. This process is called *flagging* and the respective CASA task is named `flagdata`. Basically, we remove (flag) the shadowed antennas and then with the `TFCrop` `autoflag` algorithm we flag the radio frequency interference.

In addition, data has to be corrected by the *antenna positions*. Antenna locations can be guessed through the configuration geometry or obtained from records in the NRAO database. This step is necessary because the visibility function depends on the  $u$  and  $v$  coordinates, and if the baseline positions are incorrect the resulting image will be corrupted ([VLA-Tutorial, 2016](#)).

The effects described above are independent on the calibrators. Now, using flux calibration models (see calibrators in sec. [3.3.1.1](#)), antenna gain curves and atmospheric models we calibrate our data on external sources. Those corrections are computed with the task `setjy` using the [Perley & Butler \(2013\)](#) model as flux scale. External sources are needed for an initial *phase* and *bandpass* calibration. The bandpass calibration refers to the process of measuring and correcting the frequency-dependent part of the gains. For this reason, we use bright, flat-spectrum sources with featureless spectra. On the other side, initial phase calibration permits to average over the variations of phase with time in the bandpass ([VLA-Tutorial, 2016](#)).

Next, we apply a *delay calibration* which solves antenna-based delays. The signal, which is collected at different times by the correlators, travels through wires causing a possible antenna-based delay (see eq. [6](#)).

At this point, the output of the data reduction are visually inspected, and bad spectral windows, namely those spw which are still affected by strong RFI, are manually removed from the dataset, i.e. flagged. Finally, all the calibration solutions are applied to the target and averaged in frequency and time. This final average is made with the `split` command which permits to create a new dataset with the corrected data and/or averaged data. We averaged over a time of 10 s on a number of 8 channels. This permits to create a spectrally averaged continuum data set, i.e. a spectra that only contains continuum emission.

---

<sup>16</sup>The *bandpass* is a filter, used in radio telescopes, which passes the wanted range of frequencies and attenuates those outside of it. The bandpass values are time independent.

### 3.3.3 Cleaning - Self calibration

After the external calibration has been applied to the target, it is still possible to increase the sensitivity of our image with the use of a technique named *self-calibration*.

So far, we calibrated the data using external calibrators and, finally, averaged it over a 10 s time range. However, for example, the phase calibrator is observed every  $\sim 30$  minutes and hence the phase solution are precise on this time scale. Similarly, for the amplitude correction, the primary calibrator is observed only at the beginning and at the end of the observation creating a mismatch between phase and visibility solutions. To account for this, we perform a number of rounds of self-calibration, which permits to improve the model on the target using the calibration solutions of the target itself.

In a nutshell, once a preliminary model of the source - the target -, is created, the observation is calibrated again using the same model which is then updated with a new cycle of self-calibration. After each cycle of iteration the model becomes more accurate. This permits to further calibrate the antenna-based amplitudes and phases as a function of time. Throughout this section we will see how.

**Iteration zero** To start with self-calibration we have to create an initial model, i.e. a first image, of the observation. We can see this step as the “iteration zero” of self-calibration. To reconstruct an image of the sky from the interferometer response, we have to compute the Fourier transform of the visibility (Eq. 8). In CASA, this is made using the task `clean` (Högbom, 1974), which also performs the image deconvolution. The Fourier transform of the data and deconvolution of the resulting image is computed automatically.

Deconvolution algorithms are based on sequential source removal (Ollier, 2018) which uses a mask delimiting the emission in precise areas of the sky, i.e. around the emitting objects in the observation. For this first step, we use an automatic mask around the compact and extended sources which has been created using the PYthon Blob Detector and Source Finder (PYBDSF, (Mohan & Rafferty, 2015)). We identify cleaning as the procedure to iteratively remove a fraction of the flux from the brightest pixels inside the mask of the “dirty” image, and place those in the model image. In other words, the selected components (brightness peaks) are subtracted from the visibility data to create a residual (source-subtracted) image. This cause the bright sources to be subtracted and the faint ones become visible. Therefore this require the mask to be adjusted around the new visible sources. Some important parameters characterizing the task `clean` are:

- **imsize**, the size of the image. It has to be larger than the primary beam, in order to include the primary and secondary lobes of bright sources located far from the pointing center.
- **cell**, the pixel size of the image. It has to be between  $\frac{1}{3}$  and  $\frac{1}{5}$  of the resolution of the observation to ease the deconvolution process. The approximated resolution of the observation can be retrieved by Eq. 5 using the length of the longest baseline and the observed wavelength.
- **weighting**, the type of weighting to apply to visibilities. They are used to give more importance to the information we want to get from an image. In our study we used Briggs weighting with a robust factor of zero which gives a good trade-off between resolution and sensitivity. See Briggs (1995) for a further description.

- `nterms`, the number of Taylor coefficients to model the sky frequency dependence. This takes the spectral index into account ([Rau & Cornwell, 2011](#)). We used `nterms=3`.

**Table 5:** CASA parameters and images information

	B-array	C-array	D-array
cell ("×")	$0.8 \times 0.8$	$2.5 \times 2.5$	$8 \times 8$
imsize (pixel)	9000	3072	1024
wprojplanes	512	128	64
$A_{beam}$ (pixel)	38.83	28.26	31.32
Beam size ("×")	$5.3 \times 4.2$	$13.7 \times 11.4$	$43.8 \times 40.4$
$\sigma_{rms}$ ( $\mu\text{Jy beam}^{-1}$ )	25.33	18.86	37.26

The cleaning procedure is manually stopped when all the sources have been completely subtracted, *i.e.* the residuals approach zero, and included in the model image.

**Phase only** The first iteration of self calibration starts with a new run of the `clean` task with the most updated mask from the previous run. Again, we adjust the map around the fainter sources and when the noise approaches zero we stop the task which is followed by a self-calibration.

Self calibration is a regular calibration with the target source itself as model. It enables to solve calibrators that best match the data to the model ([Self-Calibration, 2013](#)). It derives a series of gain corrections by comparing the data with their Fourier transform, the image, ([VLA-Tutorial, 2016](#)). In CASA this is computed with the task `gaincal` where, in this first iteration, we use a phase solution interval of 1 minute.

Then, the new computed model is applied with `applycal`<sup>17</sup> to the measurement set. Doing so, we prepared the corrected data to apply in the next iteration of the inversion from the Fourier transformation into the image plane (cleaning).

We are then ready to run another round of cleaning followed by a `gaincal`. However, now, we take into account phase changes on smaller scales than before. We, then, perform another phase calibration on a 30 s timescale which is subsequently applied to the corrected visibilities.

**Phase and amplitude** The phase calibrations are usually non enough to retrieve an high sensitivity on the image. This kind of calibration is not perfect, the gain solutions are interpolated from different time, and different location on the sky ([Imaging & CLEAN, 2012](#)). For this reasons a couple more of phase and amplitude `selfcal` are usually necessary.

Amplitude tends to vary more slowly than phase, so the time solutions intervals are typically larger (2 mins). The procedure to improve the source model is the same as the previous iterations, the only difference now is that we are also finding the amplitude correction factors.

If we are happy with the noise level achieved, hence it is not decreasing anymore, the final image of a single configuration is ready. The final image is obtained by combining the three configuration and

---

<sup>17</sup>[applycal task manual](#)

applying a final self-calibration with a long solution interval to align the datasets. The final image has a resolution of  $8.85'' \times 7.99''$ .

Sometimes the just described procedure is not enough to have a clear image. When bright sources are present in the image some issues can be encountered. In our data set besides the normal cleaning we applied the peeling procedure.

### 3.3.4 Peeling

The primary beam (PB) strongly affects the appearance of the synthesized image. The PB can have time-dependent or direction-dependent variations which are not corrected with the bandpass calibration.

In interferometric radio astronomical observations, bright sources can reduce the image quality if their characteristics are not fully captured by the calibration process ([Williams et al., 2019](#)). As explained in [Burke & Graham-Smith \(2009\)](#), the dirty beam responses of strong sources located in outside edges or sidelobes of the PB can produce ripples within the target field, degrading the image quality. These bright sources need an additional calibration, named *peeling*.

In our data a bright source (phase center coordinates:  $14:36:57.025 +03:24:11.668$  (J2000)) is present. To see what we mean by bright source in Fig. 2 we show how our C-configuration data looks after the first (iteration zero) cleaning iteration. The source on the right is adding noise to the overall image. In Fig. 2, we, also, evidence the pointing center, i.e. the center of the primary beam: the peeled source is extremely bright even if it is far away from the primary beam. It is now evident why sources like this disturb the image increasing the noise: in radio observations bright sources outside of the PB are not expected and for this reason the cleaning process fails. In order to proceed with the calibration that source has to be manually removed, *i.e.* it has to be peeled.

The peeling process works as a self-calibration but on a single source. During this process only a square of sky around the noisy source is cleaned - as described in sec. 3.3.3 - until the source does not produce ripples on the image anymore. At this point, we can start the cleaning on the full image again using as input the original observation with the disturbed part of the sky replaced by the one just calibrated. Furthermore, in image Fig. 3 we present the peeled and cleaned C-array image, where the noise is evidently reduced and the bright source on the right is not present anymore.

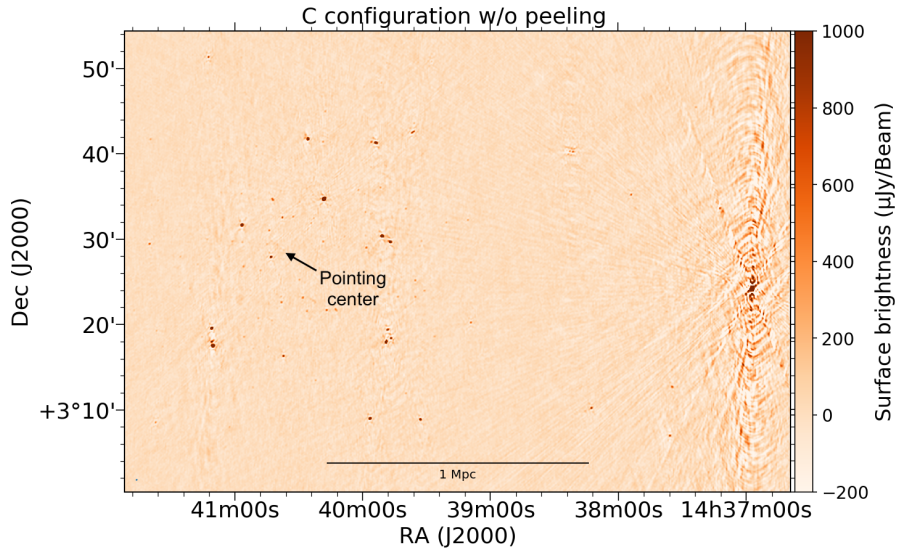


**Figure 2:** Image of the C configuration dataset after one iteration of cleaning. On the right, a bright radio source is present.

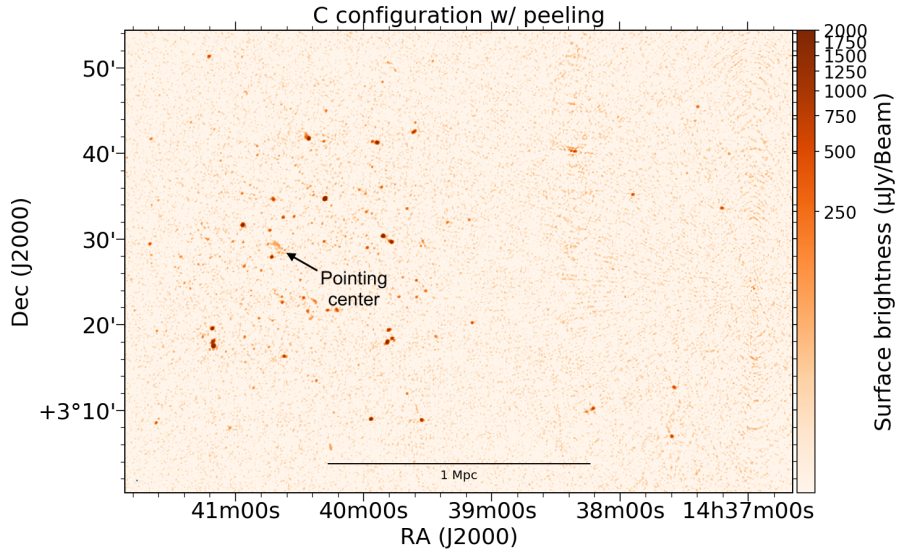


**Figure 3:** Image of the C configuration dataset after the peeling and cleaning process. In this image is easy noticeable the effect of the primary beam. The majority of the sources present in the image are around the BCG, which is also close to the *pointing center*. Moving away from the pointing center, fewer and fewer sources are visible. This is only due to the shape of the primary beam, and not to a lack of sources in that part of the sky.

## 4 Results

For viewing purposes, all the images in this work are shown with contours levels following the  $[1, 2, 4, 8, 16, 32, 64] \times \sigma_{rms}$  levels, with  $\sigma_{rms}$  the image noise of the single B-, C- and D-array configuration (see Tab. 5) and the final JVLA, GMRT and LOFAR images (Tab. 6).

### 4.1 Single configuration images

In this section, the single configuration images will be shown and described.

**B configuration:** The B-array represents the longest baseline-configuration in our observation. This configuration is sensitive to the small scales (Eq. 12), the beam size is  $5.29'' \times 4.15''$ . The absence of large scale structures is indeed evident in the top left panel in Fig. 4 where we only observe point sources. This image has beam area 38.83 pixel and  $\sigma_{rms} = 25.33 \mu\text{Jy beam}^{-1}$ .

**C configuration:** The C-array has an intermediate response to diffuse and point sources (beam size  $13.69'' \times 11.39''$ ). It is still not possible to detect the shape of the diffuse radio source present in MKW8, but the difference from the B configuration is obvious (top right panel in Fig. 4). This image has beam area 28.26 pixel and  $\sigma_{rms} = 18.86 \mu\text{Jy beam}^{-1}$ .

**D configuration:** The D-array provides the shortest baselines. Therefore, this array is sensible to high surface brightness, at the cost of angular resolution, the beam size is  $43.75'' \times 40.44''$ . With this configuration, the extension of the diffuse radio emission in MKW8 is fully detected (bottom panel in Fig. 4). This image has beam area 31.32 pixel and  $\sigma_{rms} = 37.26 \mu\text{Jy beam}^{-1}$ .

### 4.2 Final combined image

In the previous sections we briefly described the single configurations images. Each array, depending on the baseline length shows different characteristics. Combining those, we obtain an image with the surface brightness of the D-array configuration, the sensitivity on small scales of the B-array linked by an intermediate C-array configuration.

The final image is obtained by combining the data from B-, C-, D-array configurations with a final self-calibration in amplitude+phase, with a long-interval solution to align the data sets. This image is shown in the top left panel in Fig. 5 and it has  $\sigma_{rms} = 5.75 \times 10^{-5}$  and beam size  $8.85'' \times 7.99''$ . We also present the high resolution images of the same object observed with the GMRT ( $\sigma_{rms} = 4 \times 10^{-4}$  and beam size  $8.91 \times 8.56$ ) and LOFAR ( $\sigma_{rms} = 3.5 \times 10^{-4}$  and beam size  $22.45 \times 6.297$ ) telescope (top right and bottom panel in Fig. 5, respectively).

From those images we retrieve some information regarding the morphology of the diffuse source. The source extends for  $\sim 100$  kpc, i.e. an angular dimension of  $\sim 0.05$  deg. We denote that at every frequency there is a brighter spot on the northern part of the source and probably a smaller one on the southern part. The emission is therefore not uniform but filamentary. This, and the small size, typical of a radio phoenix, gives a first hint about the diffuse emission we are looking, namely, the emission does not come from a radio halo.

The optical overlay in Fig. 6 does not show an optical counterpart of the observed source meaning that we are looking at, as we already knew, diffuse emission. To understand the source context, we

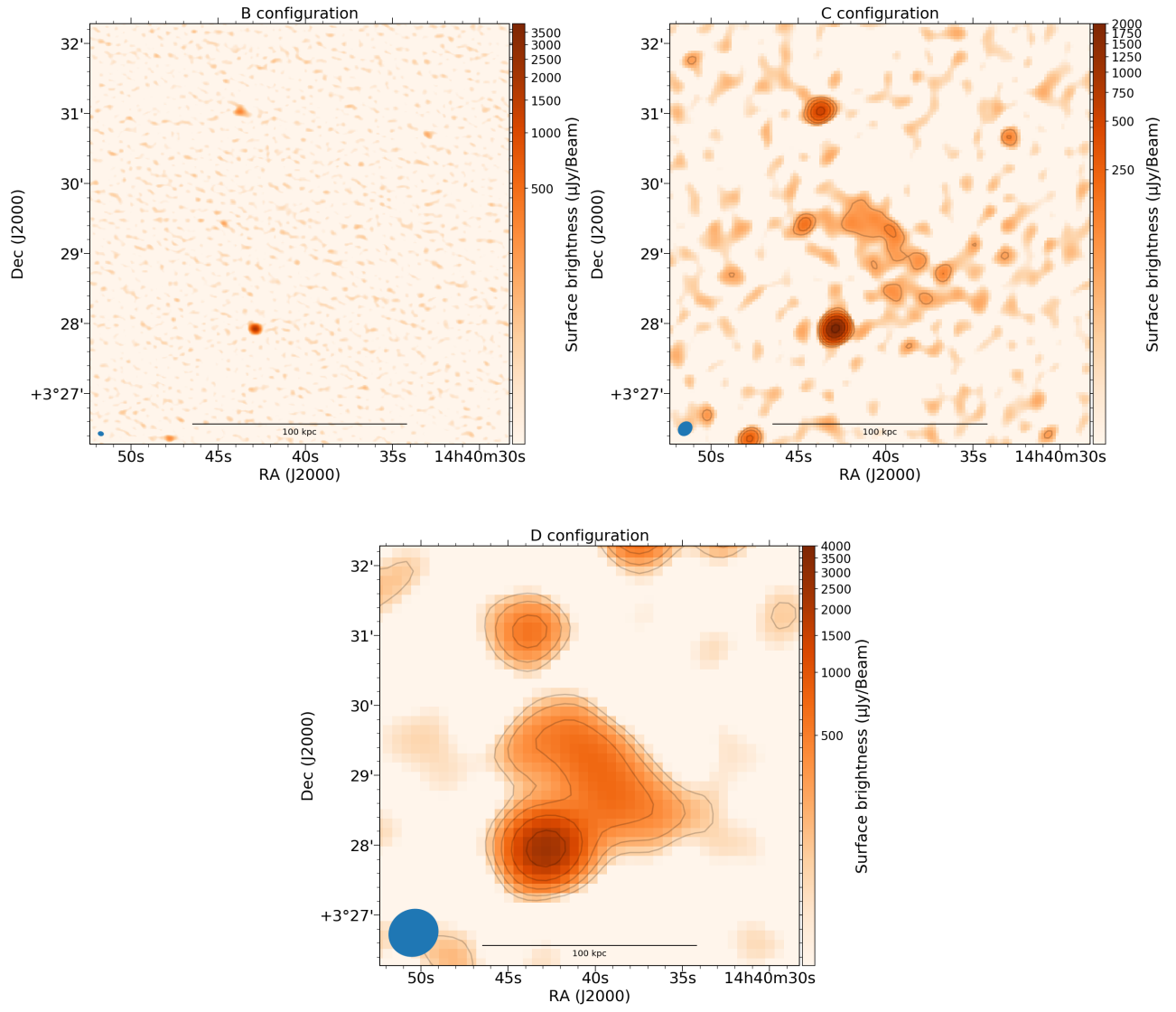


**Figure 4:** Images of the diffuse source in MKW8 taken with the B-, C- and D-array configurations of the JVLA telescope at 1.5 GHz (top left, top right and bottom panel, respectively). Contour levels are drawn at  $[1, 2, 4, 8, 16, 32, 64] \times 3\sigma_{rms}$  ( $\sigma_{rms}$  in tab. 5). The beam size (B-array:  $5.29'' \times 4.15''$ , C-array:  $13.69'' \times 11.39''$ , D-array:  $43.75'' \times 40.44''$ ) is shown in the bottom left corner of the images.

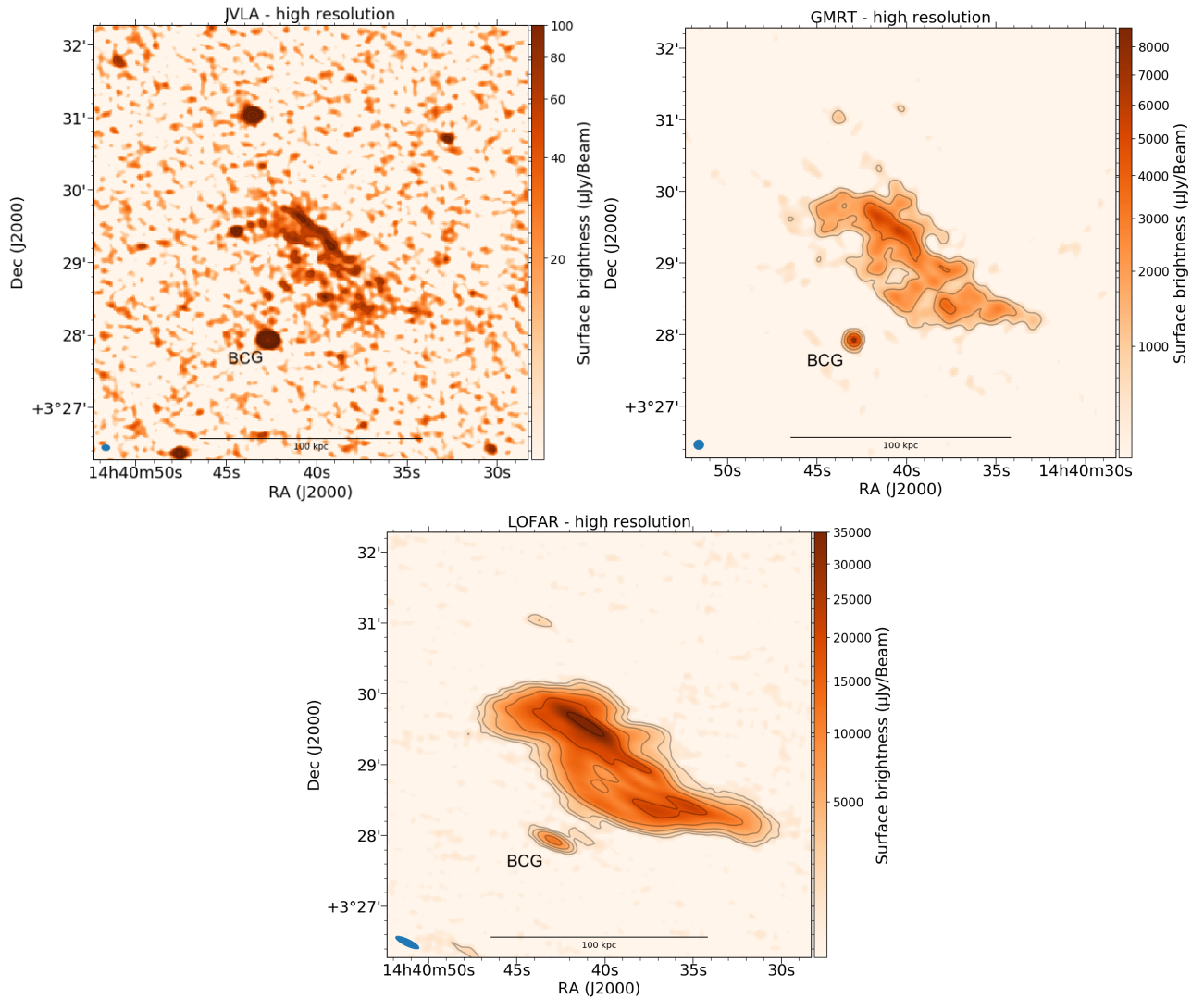


**Figure 5:** Top left: JVLA 1.5 GHz image at  $17'' \times 16''$  resolution, with  $\sigma_{rms} = 16 \mu\text{Jy beam}^{-1}$ . Top right: GMRT 325 MHz image at  $9'' \times 9''$  resolution, with  $\sigma_{rms}=250 \mu\text{Jy beam}^{-1}$ . Bottom: LOFAR 150 MHz image at  $23'' \times 7''$  resolution, with  $\sigma_{rms}=378 \mu\text{Jy beam}^{-1}$ . Contour levels are drawn at  $[1, 2, 4, 8, 16, 32, 64] \times 3\sigma_{rms}$ . The beam size is shown in the bottom left corner of each images.

present the source and its surrounding medium in Fig. 6 which shows the *Chandra* X-ray image of the full cluster and the optical zoom in the inner part of the cluster. Both images have the JVLA contours overlaid.

The apparent morphology of the X-ray emission looks roundish, the emission is not accentuated in any direction as we expect in a merging cluster. Also, the X-ray emission is peaked in the center of the cluster, where the BCG is located. The extended radio source, which is evidenced with the green contours, is located near the BCG, so we can immediately exclude it to be a radio relic: those objects are found on the outskirts of the cluster.

Moreover, the source does not follow the ICM, we have a final proof that what we are not observing an a halo.

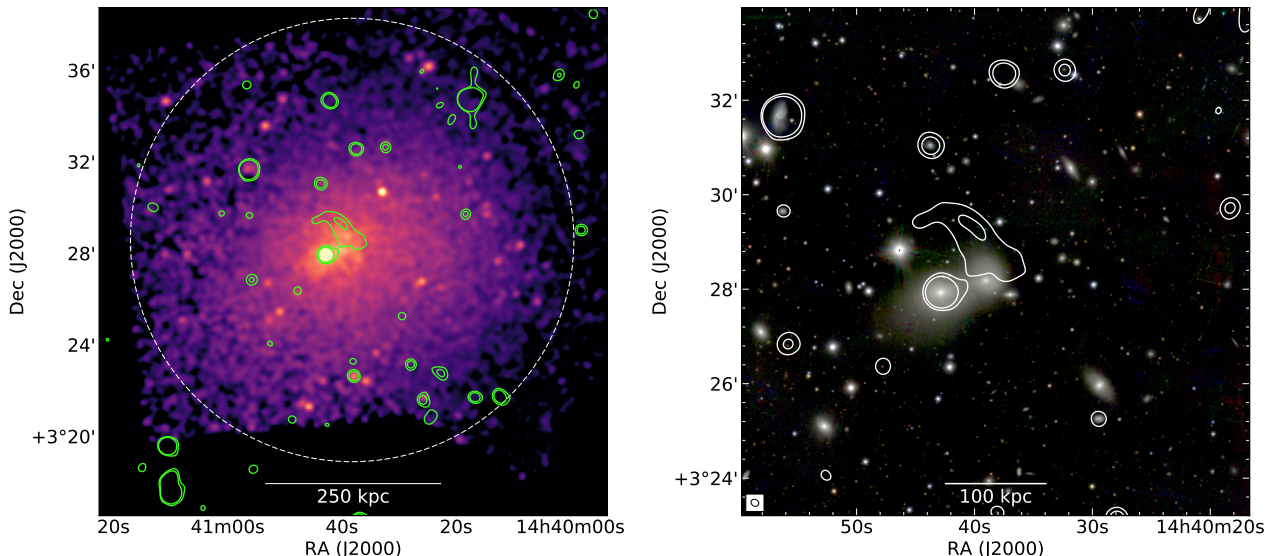


**Figure 6:** Left: Background-subtracted *Chandra* image with green contours from the JVLA at 1.5 GHz (Fig. 7) drawn at levels of  $[1, 2] \times 3\sigma_{rms}$ . The dashed circle represents  $\frac{1}{2}R_{500}$  centered on the cluster center. Right: Optical overlay with contours from the JVLA 1.5 GHz (Fig. 7) drawn at levels of  $[1, 2] \times 3\sigma_{rms}$ .

Additionally, we note that the source of interest is really close to the BCG with which might have interacted. Supposedly the BCG (more specifically, its AGN) is the source of the revived plasma.

Using the LOFAR, GMRT and JVLA images, we create spectral index maps between 150 MHz and 1.5 GHz. Using the spatial distribution of spectral indices over the extent of the source we can have insights about the origin of the diffuse emission in MKW8.

#### 4.2.1 Spectral Index Maps

As we have seen in Sec. 1.2, radio sources emit synchrotron radiation, which is well represented by a power-law spectrum ( $S \propto \nu^\alpha$ , where  $S$  the radio flux,  $\nu$  the frequency and  $\alpha$  the spectral index). Spectral index maps are created using multi-wavelength observations of the same object, or in general,

the same sky area.

Starting from Eq. 2, we want to retrieve the value of  $\alpha$ . This is possible with a simple first-order polynomial fit, where our frequency-flux relation is seen as:

$$y = ax + b. \quad (13)$$

Here, recalling Eq. 2,  $a$  is the spectral index (*i.e.* the slope of the fit),  $x$  the logarithm of the frequency  $\nu$ , and  $y$  the logarithm of the flux  $S$ .

To create a spectral index map, Eq. 13 needs to be calculated pixel by pixel.

In addition, before every calculation, the flux  $S$  for each pixel needs to be checked. We do not take the negative fluxes into account, since they do not have a psychical meaning, but only represent the noise fluctuation. Additionally, we want to exclude noisy pixel. Therefore, we blank every pixel with a brightness lower than  $3 \times \sigma_{rms}$ . Using this threshold in flux, which is decided by the user depending on the quality of the image, it is possible to exclude both types of noisy pixels. Since more images are used, the calculation is actually made only if all the pixels with the same coordinate are above the threshold, otherwise the pixel is blanked.

In order to create spectral index maps, some data processing needs to be applied to the images. First, the images used need to be aligned. More precisely, every pair of pixel, from two images, with the same  $(i,j)$  coordinates have to give information about the same part of the sky. Consequently, the images need the same amount of pixel and same pixel size.

To take the differences of each data set into account we use two **CASA** tasks, namely **imsSmooth** and **imregrid**. We use the first task to convolve all the images with a 2D Gaussian, obtaining then images with the same restoring beam size.

The beam sizes are reported in Tab. 6. Since the LOFAR image has the largest beam size, we use this as reference, *i.e.* we smoothed all the images at  $23'' \times 23''$  resolution. The task **imregrid** scales an input image to a new coordinate system using a template image. We chose as template the JVLA image.

In Fig. 7 the smoothed and regridded images of the three datasets are shown.

The way to calculate the spectral index map depends on the number of images at different frequencies are available. With two observations at two different frequencies, we use the analytical calculation of Eq. 13, otherwise a linear fit is needed.

**4.2.1.1 Analytical fit** Having two points with coordinates  $(x_1, y_1)$  and  $(x_2, y_2)$ , the slope of the line connecting them is computed using:

$$a = \frac{y_2 - y_1}{x_2 - x_1}. \quad (14)$$

This process works as well in images where pixels have coordinates  $(x, y)$ . In this way is possible to calculate the value of the spectral index for all the pixels in the radio image.

In this explanation we refer to a precise pixel using the indices notation  $i, j$ , *i.e.*  $(x_i, y_j)$ . Hence, using two images at frequencies  $\nu_1$  and  $\nu_2$ , we compute  $\alpha$  of the  $(i, j)$  pixel with Eq. 14:

$$\alpha_{i,j} = \frac{\log(S_{\nu_1,i,j}) - \log(S_{\nu_2,i,j})}{\log(\nu_1) - \log(\nu_2)} = \frac{\log\left(\frac{S_{\nu_1,i,j}}{S_{\nu_2,i,j}}\right)}{\log\left(\frac{\nu_1}{\nu_2}\right)} \quad (15)$$

with  $S_{\nu_1}$  flux at the frequency  $\nu_1$ , and  $S_{\nu_2}$  flux at  $\nu_2$ . Therefore, to create the spectral index map, we use Eq. 15 for each  $(i, j)$  pixel.

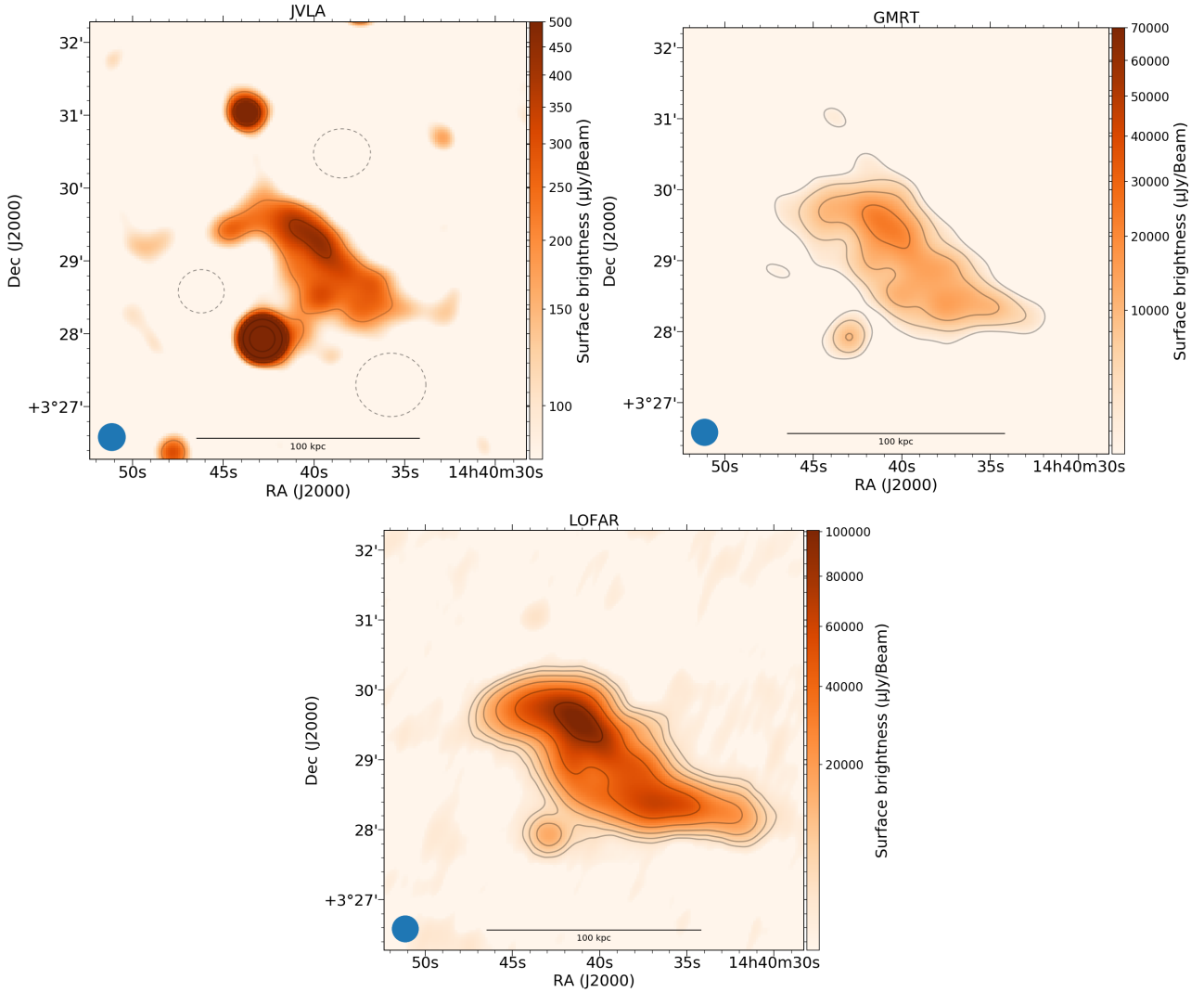


**Figure 7:** Smoothed ( $23'' \times 23''$ ) JVLA 1.5 GHZ (top left), GMRT 325 MHz (top right), and LOFAR 150 MHz (bottom) images. Contour levels are drawn at  $[1, 2, 4, 8, 16, 32, 64] \times 3\sigma_{rms}$ . In the JVLA image, the dashed circles point out some places where to retrieve the noise map. The beam size is shown in the bottom left corner of the images.

Spectral index maps are always accompanied by an error map. Every dataset has some instrumental errors. This has to be taken in account when calculating a spectral index map as we will see in the next section.

**Error estimate** The spectral index uncertainties depend solely by the uncertainties on the flux density ( $\sigma_{rms}$ ). The latter quantity,  $f$ , depends on the telescope pointing errors and imperfect calibration. In order to get the value of the noise in an image, we use the [CASA viewer](#). This stand-alone executable permits to draw regions within the display area and extract the value of the noise (rms) through the [region statistics](#). To get a proper  $\sigma_{rms}$ , the region has to be chosen sensibly. It is important to select a region not too far from the center of the primary beam and not too close to the observed source (see dashed circles on the JVLA image in Fig. 7). The noise has to belong to an area without sources but close enough to the observation target. To get an even better estimate we extract the noise in different parts of the image and compute the average. The values used to compute the error can be found in Tab. 6.

More precisely,  $\sigma_\alpha$  is calculated with the propagation of uncertainty:

$$\sigma_{\alpha,(i,j)} = \frac{1}{\ln \frac{\nu_1,(i,j)}{\nu_2,(i,j)}} \sqrt{\left( \frac{\Delta S_{\nu_1,(i,j)}}{S_{\nu_1,(i,j)}} \right)^2 + \left( \frac{\Delta S_{\nu_2,(i,j)}}{S_{\nu_2,(i,j)}} \right)^2}, \quad (16)$$

where

$$\Delta S_\nu = \sqrt{\sigma_{rms}^2 + (f S_\nu)^2} \quad (17)$$

and  $f$  is uncertainty on  $S_\nu$ .

In Fig. 8 we present the spectral index maps, and relative uncertainties, between two frequencies.

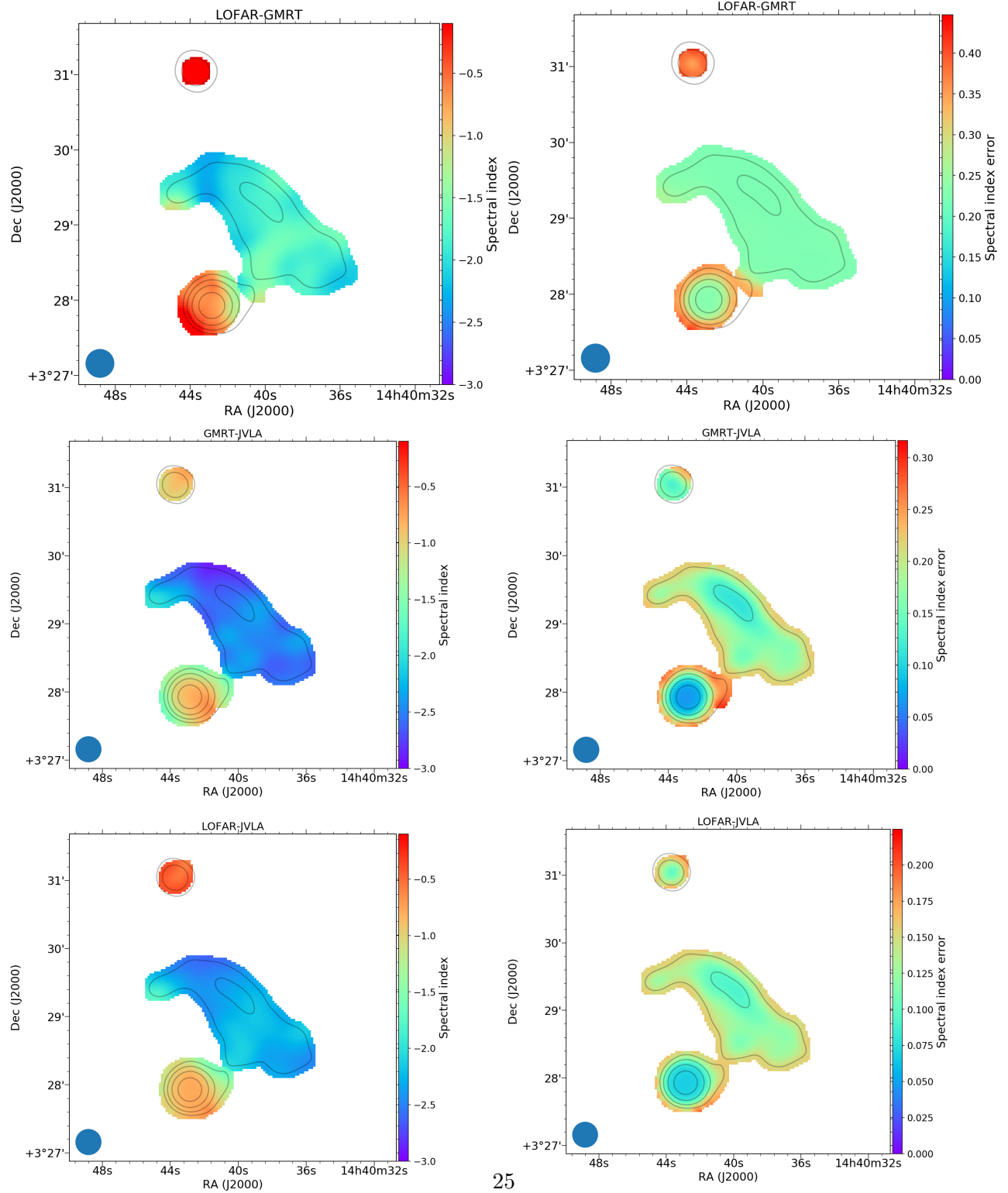
**4.2.1.2 Linear fit** Throughout this section we will discuss how to create a spectral index map with more than two observations at different frequencies.

When more than two frequencies images are available the analytical fit does not work anymore. Hence, a linear fit is used instead, since in the log-log space the synchrotron emission is linear. In practice, the slope  $\alpha$  can be easily calculated using the Python `scipy` library [optimize.curve\\_fit](#) which uses a non-linear least squares to fit a function,  $y$  (eq. 13), to the data.

**Monte Carlo error estimate** To have an estimate of the error of the linear fit we use a *Monte Carlo* simulation. We simulate the measured fluxes with a normal distribution with the correspondent uncertainty as standard deviation,  $\Delta S$ . For a number of simulations, we pick a random value from each normal distribution, check if it has a physical meaning, i.e. it is positive, and with this we calculate the value of the spectral index with the first-order polynomial fit. To generalize the result, this process, for each pixel, has to be repeated for an amount of iterations (simulations) that can be chosen by the user. In this study we decided to run the simulation for 1000 times. In the end, for each pixel in the image we have 1000 simulations of the spectral index values. The final error of a pixel is, then, the standard deviation of all the simulations based on that pixel.

We present the 150MHz-1.5 GHz image and its uncertainty map in Fig. 9. The spectral index remains approximately constant throughout the source, although we observe some variations without a precise pattern, from  $\sim -2$  to  $\sim -2.5$ . Such a steep spectra indicates that the plasma is aged and not freshly accelerated. This is opposite to what it is seen in radio relics, where an edge with young (re-)accelerated plasma (flat spectra) and a gradual steepening behind the edge is observed.

**Figure 8:** Left: spectral index maps between two frequencies, Right: error spectral index map. For both images contour levels are drawn at  $[1, 2, 4, 8, 16, 32, 64] \times 3\sigma_{rms}$ , where  $\sigma_{rms}$  is the noise map of JVLA (Fig. 7). The beam size is shown in the bottom left corner of the images.



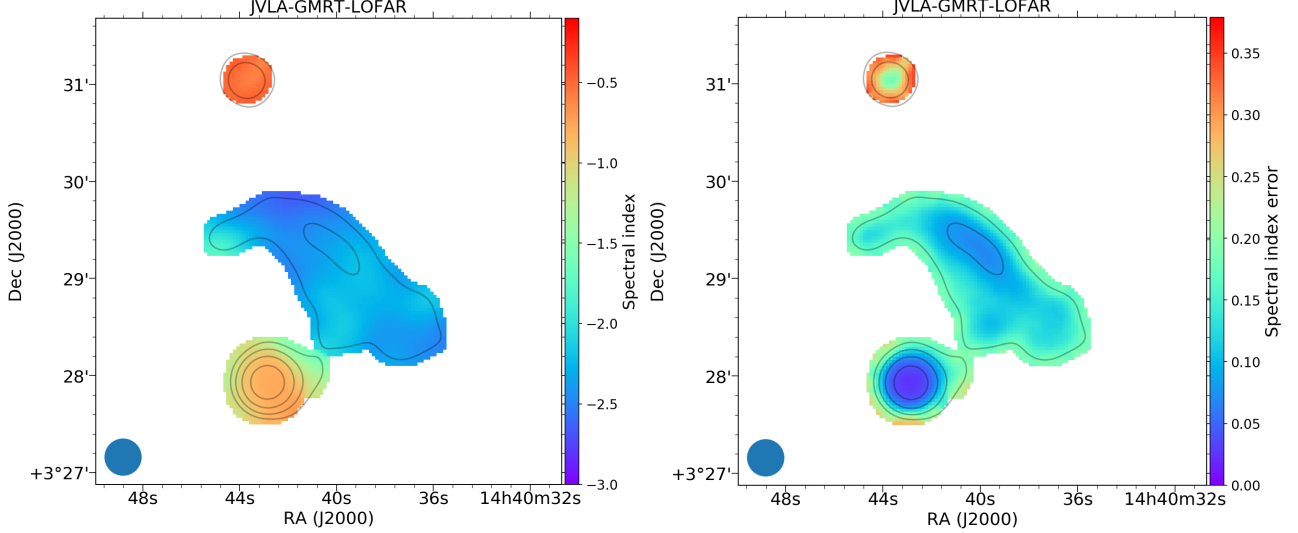


**Figure 9:** Left: 150MHz-1.5 GHz spectral index map obtained with first-order polynomial, Right: 150MHz-1.5 GHz error spectral index map. For both images contour levels are drawn at  $[1, 2, 4, 8, 16, 32, 64] \times 3\sigma_{rms}$ , where  $\sigma_{rms}$  is the noise map of JVLA (Fig.7). The beam size is shown in the bottom left corner of the images.

	LOFAR	GMRT	JVLA
$f$	15%	8%	3%
$S_{tot}$ (Jy)	1.125	$2.61 \times 10^{-1}$	$4.77 \times 10^{-3}$
$\sigma_{rms}$ (Jy)	$3.5 \times 10^{-4}$	$4 \times 10^{-4}$	$5.75 \times 10^{-5}$
$N_{point}$	6841	6841	6841
$A_{beam}$ ( $\mu\text{Jy beam}^{-1}$ )	149.851	149.851	149.851
Original Beam size ( "×")	$22.45 \times 6.297$	$8.91 \times 8.56$	$8.85 \times 7.99$
Smoothed Beam size ( "×")	$23 \times 23$	$23 \times 23$	$23 \times 23$

**Table 6:** Statistics of the smoothed and regridded images.

### 4.3 Integrated Radio Spectra

To have a rough estimate of the spectral index it is also possible to apply Eq. 15 to the total flux of a source:

$$\alpha_{\nu_1, \nu_2} = \frac{\log S_{tot, \nu_1} - \log S_{tot, \nu_2}}{\log \nu_1 - \log \nu_2} \quad (18)$$

To get the total flux of a source we use, again, the **region statistics** of **CASA viewer**. This time, we draw a contour around the steep spectra source extracting the flux ( $S_{tot}$ ), the number of pixels in the region ( $N_{points}$ ), the beam size in pixel ( $A_{beam}$ ) and the  $\sigma_{rms}$ . Those values, for each observation, are showed in Tab. 6.

Using Eq.18, we calculate the spectral index in two frequencies with an uncertainty of:

$$\sigma_\alpha = \frac{1}{\ln \frac{\nu_1}{\nu_2}} \sqrt{\left( \frac{\Delta S_{\nu_1}}{S_{\nu_1}} \right)^2 + \left( \frac{\Delta S_{\nu_2}}{S_{\nu_2}} \right)^2}, \quad (19)$$

with:

$$\Delta S_\nu = \sqrt{\sigma_{rms}^2 N_{beam} + (f \cdot S_{tot,\nu})^2}. \quad (20)$$

Here,  $\sigma_{rms}$  is the noise of the image,  $f$  is the flux scale,  $S$  the integrated flux and  $N_{beam}$  is defined as:

$$N_{beam} = \frac{N_{point}}{A_{beam}} \quad (21)$$

with  $A_{beam}$  the beam area, and  $N_{point}$  the number of pixels in the source region.

The spectra of the diffuse emission in MKW8 is shown in Fig. 10. An estimate of the curvature of the spectra can be calculated through the steepness of the line between two frequencies (Eq. 15):

- $\alpha_{150MHz}^{1.5GHz} = -2.43 \pm 0.07$
- $\alpha_{150MHz}^{325MHz} = -1.95 \pm 0.22$
- $\alpha_{325MHz}^{1.5GHz} = -2.67 \pm 0.07$

The fist-order polynomial fit with all the three frequencies, using `curve_fit`, gives an integrated  $\alpha_{150MHz}^{1.5GHz} = -2.40 \pm 0.17$ . In Fig. 10 we also plot a Jaffe & Perola ageing model (JP; [Jaffe & Perola \(1973\)](#)). This model assumes a single impulsive burst of electrons acceleration, followed by radiative losses (synchrotron emission and Inverse Compton scattering) in a constant magnetic field with a continue isotropization of the *pitch angle*, namely the angle between the magnetic field and the electron velocity vectors. In other words, this model assumes an isotropic injection of electrons which produces a power-law distribution of relativistic electrons. However, this model predicts a much stronger steepening at high frequencies than that is observed.

#### 4.4 Polarization

Magnetic fields permeate galaxy clusters and intergalactic medium on Mpc-scales changing the polarization angle of the synchrotron radiation. Those fields have an impact on the cluster evolution and history; they role the particle acceleration, influence turbulence, large-scale structure motions and formation, heat and momentum transport, etc ([van Weeren et al., 2019](#)).

Linearly polarized synchrotron emission is an important probe to study magnetic fields in cluster of galaxies. Polarization studies are useful to understand the proprieties of the magnetic field of a source. However, it is complicated to directly measure the magnetic field from the observed polarization angle and polarization fraction since those quantities are affected by Faraday rotation.

The complex linear polarization is defined as ([Sokoloff et al., 1998](#)):

$$P = Q + iU = pIe^{2i\Psi}, \quad (22)$$

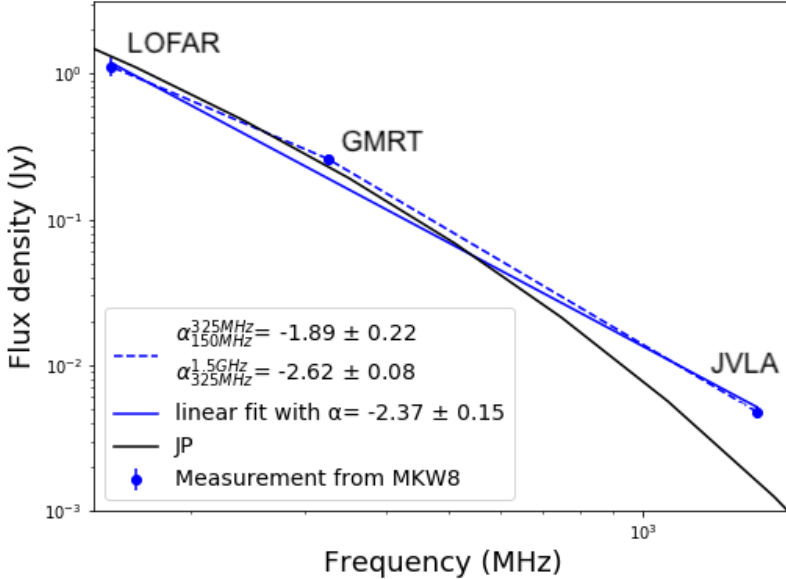


**Figure 10:** Total flux density as a function of frequency of the source. The blue points show the flux measurements at 150 MHz, 325 MHz and 1.5 GHz, the blue dashed line indicates the integrated spectral indices between two frequencies, and the blue solid line is the linear fit using the three frequencies. The black solid line represents the JP model used in [van Weeren et al. \(2012\)](#)

with  $I$ ,  $Q$  and  $U$  the measured Stokes parameters (respectively, total and orthogonal components) of the linearly polarized intensity ([Stokes, 1852](#)) and  $\Psi$  the observed polarization angle. The degree of linear polarization is:

$$p = \frac{P}{I} = \sqrt{q^2 + p^2} \quad (23)$$

where we define the fractional values  $q = Q/I$  and  $u = U/I$ . The polarization angle is:

$$\Psi = \frac{1}{2} \arctan \frac{u}{q} \quad (24)$$

Faraday rotation (FR) occurs when linearly polarized light propagates through a magneto-ionic medium causing a rotation of the polarization plane. The observed polarization angle is related to the intrinsic one ( $\Psi_0$ ) and the rotation measure (RM) as:

$$\Psi(\lambda^2) = \Psi_0 + RM\lambda^2 \quad (25)$$

Following [Burn \(1966\)](#) the RM can be written in function of the Faraday depth<sup>18</sup>:

$$\Phi = 0.81 \int_{source}^{telescope} n_e B dr \text{ (rad m}^{-2}) \quad (26)$$

<sup>18</sup>Faraday depth and RM are equal only when there is a single Faraday rotating medium with no internal Faraday rotation between the source and the observer ([Vallee \(1980\)](#) and [Brentjens, M. A. & de Bruyn, A. G. \(2005\)](#))

with  $n_e$  the free electron density ( $\text{cm}^{-3}$ ),  $\mathbf{B}$  the magnetic field in ( $\mu\text{G}$ ) and  $\mathbf{r}$  an infinitesimal path length along the line of sight (in parsec).

The measured Stokes Visibilities are, by definition, complex numbers and are related to the real source brightness through a Fourier transform. The total intensity,  $I$ , image is shown in Fig. 5. To obtain the intrinsic polarization angle we need to fit eq. 26, so at least two *lambda* (or observing frequencies) are required of Stokes  $U$  and  $Q$  images. Hence, this is done by dividing the wideband observation into small pieces (i.e. narrow band) and producing a number of narrow-band images with the widefield imager `wsclean` (Offringa et al., 2014). Those images are the input of the Rotation Measure (RM) Synthesis technique, first described by Burn (1966) and implemented by Brentjens, M. A. & de Bruyn, A. G. (2005). In this approach, the Fourier transform is computed using a sampling function introduced by Brentjens, M. A. & de Bruyn, A. G. (2005), which is non-zero only at values of  $\lambda^2$  which are sampled by the telescope. The RM-Synthesis technique is run by means of the `rmsynthesis` pipeline.

The images created with `rmsynthesis` do not show a clear presence of a polarized emission. Given its definition (Eq. 23), the polarized intensity is always positive, also in case of no emission in the Stokes  $Q$  and  $U$ . Theoretically, to find the degree of polarization on the source we can subtract the flux of the source by the flux of a empty region with the same amount of pixel in the polarization image. To do so, we use a method which involves both linear and total polarization images. Using those is possible to compute the 'zero' ( $p_{diff}$ ) in the polarization:

$$p_{diff} = S_{source} - S_{empty} \frac{\#\text{pixel source}}{\#\text{pixel empty}} \quad (27)$$

Where we call  $S_{source}$  the flux inside the region containing the source in the total polarization image,  $S_{empty}$  the flux inside an empty - without emitting sources - region in the `polint` image and as  $\#\text{pixel source}$  and  $\#\text{pixel empty}$  the amount of pixels in those regions. Having this value, the upper limit of the polarization is the difference between the flux of the region where the source lays and the 'zero'. Following this procedure we got an upper limit in polarization of 0.8%.

## 5 Discussion

In this work, we have presented a multi-wavelength study of an ultra-steep spectrum diffuse radio source in the galaxy cluster MKW8. In literature we do not find previous spectral index studies. For this reason, our discussion will be based on comparison with simulations or similar sources.

Diffuse radio sources with irregular morphology reached more interest in the scientific community since new and upgraded low-frequency radio telescopes are available and hence it is possible to reveal, and therefore study, more of those steep-spectrum sources. However, when observing at clusters at low enough frequencies, halos and cluster radio shocks will fuse with old AGN radio plasma regions rendering the diffuse emission sources classification complicated (van Weeren et al., 2019). Also, those kind of emitters are difficult to observe because of their short radiative life time ( $\sim 10$  Myrs at GHz frequencies) (Mandal et al., 2019).

Usually (e.g. Slee et al. (2001)) relics and phoenixes show a variety of fine structures that takes the form of arcs, filaments and loops of enhanced surface brightness. In our source we denote some filaments following the phoenix length. Those are distinguishable in the high resolution images in Fig. 5. In sec. 4.2, we, already, excluded the possibility of a radio halo or relic. Throughout this section we will further discuss the classification of the MKW8's diffuse radio source.

Radio phoenixes are aged plasma (radio galaxy lobes) whose emission is boosted by adiabatic compression of merging shocks. This scenario has been proposed and simulated by Enßlin & Brüggen (2001), Enßlin & Brüggen (2002), Enßlin, T. A. & Gopal-Krishna (2001). In addition, recently, Nolting et al. (2019) simulated that cluster radio galaxy tails passing through ICM shocks, or with large relative motion, show a filamentary morphology, ultra-steep and curved spectra. Furthermore, there is evidence of this kind of sources in literature, as Slee et al. (2001), de Gasperin et al. (2015),(van Weeren, R. J. et al., 2011).

In particular, Slee et al. (2001) studied the diffuse radio emission in A133 which shows similar characteristics to our source. Their source shows an extremely steep spectrum, also, a part of it seems connected to the BCG (cD galaxy) at the center of the cluster and it also revealed a low fractional polarization. Even the MKW8's source is close to the BCG with which might interacted, but no there is not a clear "bridge" that seems to connect it to the BCG. In A133 Rizza et al. (2000) interpret the narrow bridge between the diffuse emission and the galaxy as a perturbed jet propagating through a cooling flow which then creates an amorphous radio lobe. This filament is not evident in Slee et al. (2001)'s A133 higher resolution image, however, the steep radio spectra made them categorize the source as a radio relic<sup>19</sup>.

Radio phoenixes close to the cluster center, as observed by Enßlin, T. A. & Gopal-Krishna (2001), are sources expected to have a very steep spectrum and a high surface brightness at low frequencies. In our case, the integrated spectral index retrieved  $\alpha_{150MHz}^{1.5GHz} = -2.40 \pm 0.17$  and the average of the intermediate spectral indices (150 Mhz-325 Mhz; 325 MHz-1.5 GHz; 150 Mhz-1.5 GHz)  $\bar{\alpha} = -2.35 \pm 0.04$ . The intermediate spectral indices, as indicated in Fig. 10, have values  $\alpha_{150MHz}^{325MHz} = -1.95 \pm 0.22$  and

<sup>19</sup>The name radio phoenix has been introduced later. Now that the name phoenix made its way in literature, the sources studied by Slee et al. (2001) can be named as phoenix.

$\alpha_{325MHz}^{1.5MHz} = -2.67 \pm 0.07$  which indicates a curvature of the spectra. With the 150 MHz-325MHz-1.5 GHz spectral index map (Fig. 9) we do not detect clear substructures, throughout the structure the spectral index ranges from  $\sim -2.5$  to  $\sim -2$ . Only the North-Eastern part of the relic has a  $\alpha > -2$ . With such a steep spectra, we are not observing young and freshly accelerated plasma. The proximity to the BCG can be explained in two ways. Either the steep spectra source is close to the BCG, which injected radio plasma, that has been then revived, or the source looks close to the BCG only because of projection effects.

MKW8 is located in a moderately massive cluster ( $M_{500} < 10^{15} M_\odot$ ). [Mandal et al. \(2019\)](#) discussed that most of the previously discovered radio phoenix candidates are most likely found in non-massive clusters within a radius smaller than  $R_{500}$ . From the X-ray overlay (Fig. 6 left) this is clearly true.

We did not observe polarized emission from the diffuse radio source in MKW8. It is possible that the source it is intrinsically not polarized, or since it's located in the cluster center it suffers an extremely depolarization due to the ICM. The flux of the source is low meaning that the mechanism which re-accelerated the electrons was not powerful enough to align the E-vectors.

It is worth remembering that having radio (synchrotron) emission means that there is a magnetic field. So, it is important to clarify that a lack in polarization in the observation images does not mean a lack in magnetic field. The low polarization could be due to tangled fields <sup>20</sup> and/or Faraday depolarization <sup>21</sup>.

MKW8's source is not a relic because there is no association with a shock wave from the Xray; it's not a halo because it's small in size and doesn't follow the Xray emission. We classify it as a phoenix because of the irregular, filamentary shape, because the cluster is not extremely massive, and because is characterized by a ultra steep spectral index.

---

<sup>20</sup>With tangled fields we denote magnetic fields with an higher contribution from the random component,  $B_r$ , than the uniform one  $B_0$ . Therefore, the randomness of the field leads to an overall null magnetic field.

<sup>21</sup>The radiation from an extended synchrotron source which travels through an ionized medium has the rotation measure that depends on (eq. 26) the electron density and the magnetic field encountered in the LOS. Therefore, the measured radiation, even if highly polarized when emitted, can be reduced by medium among the propagation path.

## 6 Conclusion

The purpose of this study was to understand the nature of the steep-spectrum source (emitting plasma) observed in the MKW8 cluster. This plasma extends for  $\sim 150$  kpc and is located near the brightest cluster galaxy (BCG). We managed to have three full resolution images of JVLA, LOFAR and GMRT (Fig. 5) which are discussed in sec. 4.2. We also attempted to study the morphology and spectral properties of the source. The integrated spectral index has a value  $\alpha_{150MHz}^{1.5GHz} = -2.40 \pm 0.17$ . The spectral index map shows an almost uniform spectral index with a value comprised between  $\sim -2.5$  and  $\sim -2$ .

The source it is not polarized, more precisely we found an upper limit for the polarization of 0.8%. In sec. 5 we explained why we expect this source to be a radio phoenix, *i.e.* fossil radio plasma from a previous episode of AGN activity which has been revived by a merging shock. Given all the characteristics (i) small size; (ii) centrally located in the cluster so its history is probably related to the AGN fossil radio plasma; (iii) filamentary structure; (iv) ultra steep spectrum; we classify this source as a radio phoenix.

## References

- Beers, T. C., Kriessler, J. R., Bird, C. M., & Huchra, J. P. 1995, , 109, 874
- Bharadwaj, V., Reiprich, T. H., Schellenberger, G., et al. 2014, *Astronomy & Astrophysics*, 572, A46
- Blumenthal, G. R., Faber, S. M., Primack, J. R., & Rees, M. J. 1984, , 311, 517
- Brentjens, M. A. & de Bruyn, A. G. 2005, *A&A*, 441, 1217
- Briggs, D. S. 1995, in American Astronomical Society Meeting Abstracts, Vol. 187, American Astronomical Society Meeting Abstracts, 112.02
- Brunetti, G. & Jones, T. W. 2014, *International Journal of Modern Physics D*, 23, 1430007
- Burke, B. F. & Graham-Smith, F. 2009, *An Introduction to Radio Astronomy*, 3rd edn. (Cambridge University Press)
- Burn, B. J. 1966, , 133, 67
- Burns, J. O. 1990, , 99, 14
- Cassano, R., Ettori, S., Giacintucci, S., et al. 2010, *The Astrophysical Journal*, 721, L82
- Cuciti, V., Cassano, R., Brunetti, G., et al. 2015, *Astronomy & Astrophysics*, 580, A97
- de Gasperin, F., Oglean, G. A., van Weeren, R. J., et al. 2015, , 448, 2197
- De Young, D. S. 1984, , 111, 373
- Diaferio, A. 1999, , 309, 610
- Elkholy, T. Y., Bautz, M. W., & Canizares, C. R. 2015, *The Astrophysical Journal*, 805, 3
- Enßlin, T. A. & Brüggen, M. 2001, in *Clusters of Galaxies and the High Redshift Universe Observed in X-rays*, ed. D. M. Neumann & J. T. V. Tran, 58
- Enßlin, T. A. & Brüggen, M. 2002, , 331, 1011
- Enßlin, T. A. & Gopal-Krishna. 2001, *A&A*, 366, 26
- Feretti, L. 2005, *Advances in Space Research*, 36, 729
- Feretti, L. & Giovannini, G. 1996, *Symposium - International Astronomical Union*, 175, 333–338
- Feretti, L., Giovannini, G., Govoni, F., & Murgia, M. 2012, , 20, 54
- Forman, W. & Jones, C. 1982, , 20, 547
- Gitti, M. 2015, in *The Many Facets of Extragalactic Radio Surveys: Towards New Scientific Challenges*, 43

- Govoni, F., Feretti, L., Giovannini, G., et al. 2001, , 376, 803
- Gupta, Y., Ajithkumar, B., Kale, H., et al. 2017, Current Science, 113, 707
- Högbom, J. A. 1974, , 15, 417
- Hudson, D. S., Mittal, R., Reiprich, T. H., et al. 2010, Astronomy and Astrophysics, 513, A37
- Imaging, R. & CLEAN. 2012, Radio Imaging and CLEAN
- Jaffe, W. J. & Perola, G. C. 1973, , 26, 423
- Kale, R., Venturi, T., Giacintucci, S., et al. 2015, A&A, 579, A92
- Katayama, H., Hayashida, K., Takahara, F., & Fujita, Y. 2003, The Astrophysical Journal, 585, 687
- Kempner, Reiprich, T., Joshua, & Soker, N. 2004
- Komissarov, S. & Gubanov, A. 1994, Astronomy and Astrophysics, 285, 27
- Kravtsov, A. V. & Borgani, S. 2012, , 50, 353
- Lin, Y. & Mohr, J. J. 2004, The Astrophysical Journal, 617, 879–895
- Mandal, S., Intema, H. T., Shimwell, T. W., et al. 2019, , 622, A22
- Mandal, S., Intema, H. T., van Weeren, R. J., et al. 2019, Revived Fossil Plasma Sources in Galaxy Clusters
- Markevitch, M. & Vikhlinin, A. 2007, , 443, 1
- McMullin, J. P., Waters, B., Schiebel, D., Young, W., & Golap, K. 2007, Astronomical Society of the Pacific Conference Series, Vol. 376, CASA Architecture and Applications, ed. R. A. Shaw, F. Hill, & D. J. Bell, 127
- Miniati, F., Ryu, D., Kang, H., et al. 2000, Astrophys. J., 542, 608
- Mitchell, R. J., Culhane, J. L., Davison, P. J. N., & Ives, J. C. 1976, , 175, 29P
- Mohan, N. & Rafferty, D. 2015, PyBDSF: Python Blob Detection and Source Finder, Astrophysics Source Code Library
- Nolting, C., Jones, T. W., O'Neill, B. J., & Mendygral, P. J. 2019, , 885, 80
- Offringa, A. R., McKinley, B., Hurley-Walker, N., et al. 2014, Monthly Notices of the Royal Astronomical Society, 444, 606–619
- Ollier, V. 2018, PhD thesis
- Olmi, L. 2002, Astronomical Society of the Pacific Conference Series, Vol. 278, The Effects of the Atmosphere, ed. S. Stanimirovic, D. Altschuler, P. Goldsmith, & C. Salter, 413–432

- Perley, R. A. & Butler, B. J. 2013, , 204, 19
- Perley, R. A., Chandler, C. J., Butler, B. J., & Wrobel, J. M. 2011, , 739, L1
- Piffaretti, R., Arnaud, M., Pratt, G. W., Pointecouteau, E., & Melin, J.-B. 2011, *Astronomy Astrophysics*, 534, A109
- Press, W. H. & Schechter, P. 1974, , 187, 425
- Rau, U. & Cornwell, T. J. 2011, *Astronomy Astrophysics*, 532, A71
- Reiprich, T. H. & Bohringer, H. 2002, *The Astrophysical Journal*, 567, 716–740
- Rizza, E., Loken, C., Bliton, M., et al. 2000, , 119, 21
- Rybicki, G. B. & Lightman, A. P. 1979, *Radiative processes in astrophysics*
- Self-Calibration. 2013, Self-Calibration
- Slee, O. B., Roy, A. L., Murgia, M., Andernach, H., & Ehle, M. 2001, *The Astronomical Journal*, 122, 1172
- Sokoloff, D. D., Bykov, A. A., Shukurov, A., et al. 1998, , 299, 189
- Springel, V., Frenk, C. S., & White, S. D. M. 2006, , 440, 1137
- Stokes, G. G. 1852, *Philosophical Transactions of the Royal Society of London Series I*, 142, 463
- Sun, M. 2009, , 704, 1586
- Tümer, A., Tombesi, F., Bourdin, H., et al. 2019, *Astronomy Astrophysics*, 629, A82
- Vallee, J. P. 1980, , 86, 251
- van Haarlem, M. P., Wise, M. W., Gunst, A. W., et al. 2013, *A&A*, 556, A2
- van Weeren, R. J., de Gasperin, F., Akamatsu, H., et al. 2019, *Space Science Reviews*, 215
- van Weeren, R. J., Röttgering, H. J. A., Intema, H. T., et al. 2012, *Astronomy Astrophysics*, 546, A124
- van Weeren, R. J., Röttgering, H. J. A., & Brüggen, M. 2011, *A&A*, 527, A114
- VLA-Tutorial. 2016, VLA Continuum Tutorial 3C391-CASA4.6
- Von Der Linden, A., Best, P. N., Kauffmann, G., & White, S. D. M. 2007, *Monthly Notices of the Royal Astronomical Society*, 379, 867
- Williams, P. K. G., Allers, K. N., Biller, B. A., & Vos, J. 2019, *Research Notes of the AAS*, 3, 110
- Zhang, Y.-Y., Andernach, H., Caretta, C. A., et al. 2011, *Astronomy Astrophysics*, 526, A105